NANO · MICRO small
www.small-journal.com

Boosting Photoconductivity by Increasing the Structural Complexity of Multivariate Covalent Organic Frameworks

Marta Gordo-Lozano, Marcos Martínez-Fernández, Rajendra Prasad Paitandi, José I. Martínez, José L. Segura, and Shu Seki**

The assessment of the photoconductivity of Donor-Acceptor (D-A) ordered bulk heterojunctions is gaining attention for the development of innovative organic semiconductors in optoelectronics. Here, the synthesis of pyrene-based (D) Covalent Organic Frameworks, achieve through a multivariate reaction involving two distinct acceptors is reported (A). The products are characterized using powder x-ray diffraction, N_2 sorption isotherms, electronic microscopy, and *in silico* calculations, among other techniques. These characterizations reveal that the multicomponent synthesis enables the modification of properties (e.g., bandgap) of the framework while preserving its structural features, such as crystallinity and porosity. The ordered D-A arrays position these materials as promising candidates for photoconductive semiconductors, particularly regarding the variation in the composition of isotopological frameworks. Photoconductivity experiments demonstrate a volcano-type correlation with respect to the A moiety content, with the optimal value reaching 7.9×10^{-5} cm^2 V^{-1} s^{-1} for the bare NIP$_{25\%}$-COF. This study illustrates how introducing diverse acceptor units through multivariate synthesis can enhance the photoconductivity of these materials via "defect" engineering, without sacrificing their crystalline or porous characteristics and avoiding the need for *de novo* synthesis.

1. Introduction

In the past decades, porous frameworks have revolutionized the field of materials in areas such as adsorption,[1] catalysis[2] or batteries[3] since their insoluble and non-fusible character has put them in the spotlight for heterogeneous applications.[4] Among them, Covalent Organic Frameworks (COFs) are a special kind of crystalline and porous polymers, built-up from lightweight atoms organized in a hierarchically organized structure.[5] One of the most noteworthy attributes of these frameworks is the pre-designability of the network, as well as the pore wall interface, offering the ability to create bespoke materials with tunable properties.[6] The tunability of the network can be performed following two strategies: *post-* or *pre*-synthetically, showing complementary advantages.[7] Among the *pre*-synthetic strategies, the multivariate (or multi-component) reactions are emerging as a convenient *one pot* approach to modify the organic backbone avoiding potential range order or porosity loss that may occur in post-synthetic modification.[8] The conventional multi-component reaction involves the concerted formation of different linkages[9] or at least, the reaction between three different molecules.[10] Following this concept, the crystallization of COFs with increased pore complexity has been achieved.[5a]

Beyond the interest of the pore surface tunability, it has been demonstrated previously that the integration of two different accepting (A) or donating (D) units in the same material has a critical impact on the optical properties.[11] For that reason, we envisaged that by using the multivariate approach the modulation of the optoelectronic properties of isostructural frameworks could be achieved.[10e] Thus, the obtainment of different framework materials with identical topology and crystal morphology makes this strategy a good approach to compare applications such as photoconductivity, since small variations in the crystalline phase could influence the exciton migration processes.[6c,12]

Photoconductivity is the physical phenomenon where a material becomes electrically conductive upon irradiation with an electromagnetic field.[13a] Thus, the photoinduced charge carrier generation and the carrier transport are the main requirements to obtain photoconductive materials with great interest in areas such

M. Gordo-Lozano, M. Martínez-Fernández, J. L. Segura
Facultad de CC. Químicas
Universidad Complutense de Madrid
Avenida Complutense s/n, Madrid 28040, Spain
E-mail: segura@ucm.es

R. P. Paitandi, S. Seki
Graduate School of Engineering
Kyoto University
Nishikyo-ku, Kyoto 615–8510, Japan
E-mail: seki@moleng.kyoto-u.ac.jp

J. I. Martínez
Departamento de Sistemas de Baja Dimensionalidad
Instituto de Ciencia de Materiales de Madrid (ICMM-CSIC)
Madrid 28049, Spain

The ORCID identification number(s) for the author(s) of this article can be found under https://doi.org/10.1002/smll.202406211

DOI: 10.1002/smll.202406211

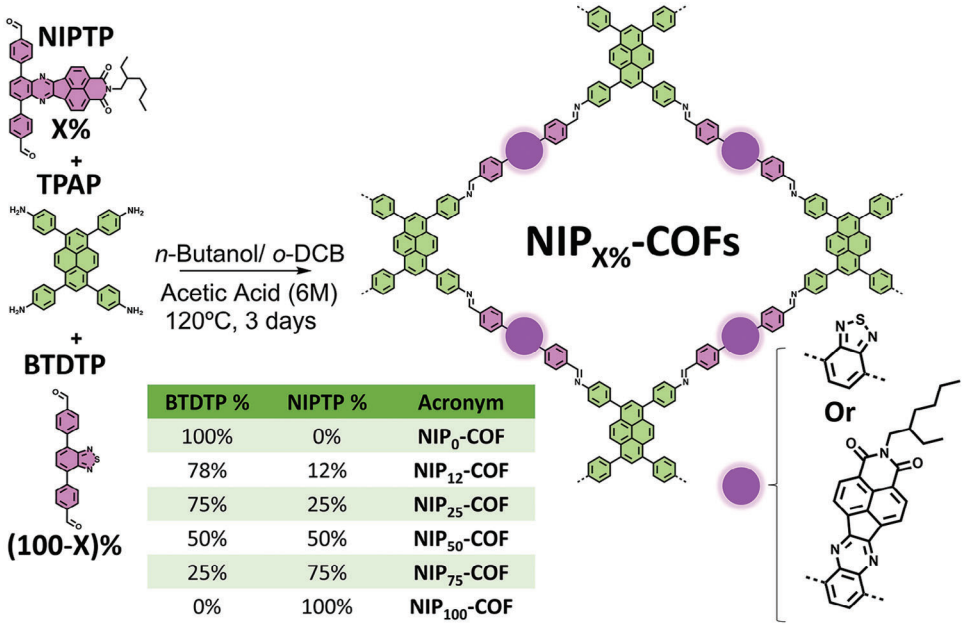

BTDTP %	NIPTP %	Acronym
100%	0%	NIP_0-COF
78%	12%	NIP_{12}-COF
75%	25%	NIP_{25}-COF
50%	50%	NIP_{50}-COF
25%	75%	NIP_{75}-COF
0%	100%	NIP_{100}-COF

Scheme 1. General synthesis procedure of **$NIP_{X\%}$-COFs**.

as organic solar cells or photovoltaics.[13] In this field, most of the photoconductive materials are produced by the self-assembly of organic molecules combining electron donor and acceptor moieties to build a bulk heterojunction.[14]Despite the great efforts in controlling the assembly processes, the atomic control of the heterojunction interfaces would be a major milestone.[13d,11c,15] In addition, the enhancement of photoconductivity by the introduction of structural defects is emerging as a powerful tool to develop new technological possibilities by: i) the band-gap reduction and ii) the electron-hole separation.[6c,11c,12a,16a] In this sense, COFs with their inherent crystallinity, have been already employed for the evaluation of the photoconductive processes.[12a,16] However, the modulation of the conductivity values by employing the three-component synthesis is still unexplored. Therefore, we anticipate that the multivariate synthesis of COFs represents a straightforward method to enhance the structural diversity. On the one hand, this approach allows for fine-tuning of the optoelectronic properties and energy levels of the materials, optimizing charge transport pathways.[12a] On the other hand, one of the linkers could be employed in small amounts as a "dopant" (defect), serving as a site for charge localization or electron-hole separation.[6c,16a,17] These variables could adjust the photoconductivity behavior of COFs with identical morphology, resulting in optimized photoconductive properties for specific applications (e.g., photovoltaics or organic solar cells).[4,11c,12b,c,13]

Herein, we report the three-component synthesis of a **$NIP_{X\%}$-COFs**, synthesized through the reaction of **BTDTP** and **NIPTP** in varying proportions, interconnected by **TPAP** as an electron-rich tetragonal unit with the aim to enhance light adsorption and charge transport (**Scheme 1**).[18] Thus, the family of **$NIP_{X\%}$-COFs** will display different Donor-Acceptor (D-A) properties depending on the relative content of the **BTDTP** and **NIPTP** units, essential for the band-gap modulation and electron-hole separation.[11b,15b] Finally, the photoconductivity was studied upon irradiation with a 355 nm laser pulse, revealing that the optimal NIP percentage is 25% (**$NIP_{25\%}$-COF**). These results indicate that the photoconductivity of isostructural COFs can be pre-synthetically enhanced by the introduction of structural defects using three-component reactions.

2. Results and Discussion

2.1. Synthesis and Characterization

The **BTDTP** linker was synthesized as previously described[19] (Scheme S1, Supporting Information), while the synthesis of the **TPAP** linker was optimized using microwave synthesis based on a previously described protocol,[20] enabling us to achieve higher yields of this tetraamine within a 2 h reaction time (Scheme S2, Supporting Information). Finally, the novel **NIPTP** was synthesized similarly by employing the **NID** intermediate previously described by us (Schemes S3 and S4, Supporting Information).[21] Finally, the targeted **$NIP_{X\%}$-COFs**, with varied proportions of the aldehyde-containing linkers, were performed via the solvothermal Schiff's base condensation reaction catalyzed by aqueous acetic acid (6M), leading to the formation of a family of isotopological frameworks but with different organic compositions.[15b] The amounts of the **NIPTP** units correspond to the ideal number of novel moieties per pore, as determined by the previously described formula (% = n/sides of the expected geometric form).[22] For this study, the initial values of "n" were 0, ½, and 1 (**$NIP_{X\%}$-COFs** with X = 0, 12, and 25%) to investigate the effects of "doping" a photoconductive structure. Given the promising results (*vide infra*) in enhancing photoconductivity, we also synthesize the COFs with "n" = 2, 3, and 4 (**$NIP_{X\%}$-COFs** with X = 50, 75, and 100%) to systematically examine the effect of having one-half, one, two, three and four naphtaleneimide units per pore statistically. This approach allowed us to study the influence of NIP

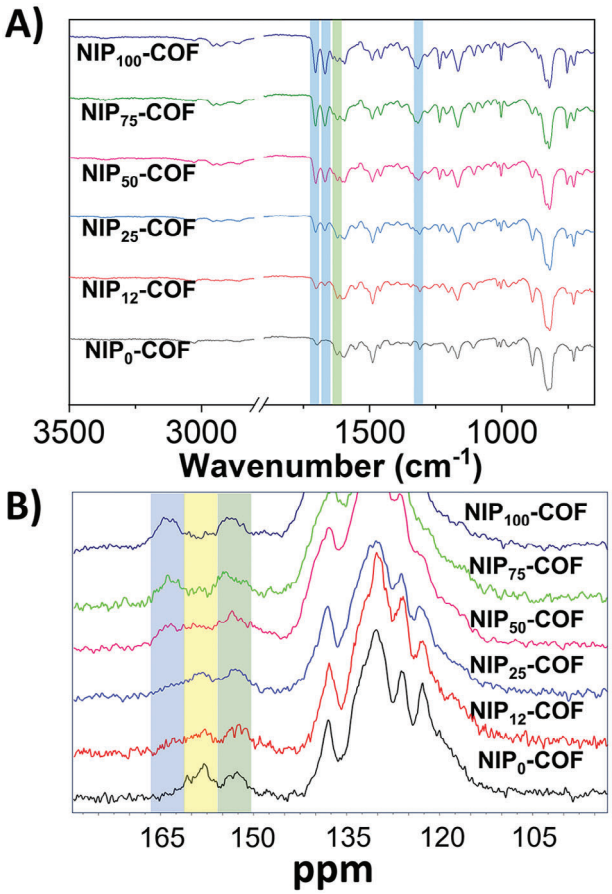

Figure 1. A) Comparison of FTIR spectra of **NIP$_{X\%}$-COFs**. B) ^{13}C-CP-MAS-NMR spectra of **NIP$_{X\%}$-COFs** in the 170–100 ppm range.

in varying proportions on the photoconductivity. As per our standard protocol, we began with experiments using low proportions of the new unit **NIPTP** to validate the multicomponent synthesis within the three-component synthesis, gradually increasing the proportion to assess its impact on reactivity, crystallinity, and other key properties. For clarity, all characterizations will be presented systematically throughout the article.

Fourier Transform Infrared (FTIR) spectroscopy (**Figure 1A**) was utilized to monitor the advancement of the polymerizations. The efficacy of the Schiff's base condensations (Figures S1–S7, Supporting Information) was validated by the disappearance of the signals corresponding to the aldehyde groups (1697 cm^{-1}) and amine functionalities (3451 and 3359 cm^{-1}), leading to the emergence of imine signals (≈1623 cm^{-1}, highlighted in green) in all synthesized frameworks. As expected, with the increasing content of the **NIPTP** unit, the imide stretching at ≈1704, 1666 and 1317 cm^{-1} (highlighted in blue) gradually increases in intensity, without the presence of the aldehyde signals, confirming the incorporation of the rylenimide moieties (Figure 1A) in the extended frameworks. Additionally,[13] cross-polarization magic angle spinning nuclear magnetic resonance (^{13}C-NMR-CP-MAS) spectra (Figure 1B; Figures S8–S14, Supporting Information) confirm the formation of imine linkages with signals ≈153 ppm (green band) for all COFs, with no additional aldehyde signals (≈190 ppm). In good agreement with the FTIR experiments, as the amount of **NIPTP** increases, the signals for the six-membered imide (C=O) gradually appear at 163 ppm (highlighted in blue) while the characteristic benzothiadiazole (C=N) signals at ≈158 ppm fade (highlighted in yellow).[4a]

Additionally, signals between 142 and 117 ppm are attributed to aromatic fragments within the aromatic framework. Lastly, signals between 45 and 14 ppm are associated with alkyl chains of the **NIPTP** moiety, with intensities increasing as the linker content increases, consistent with the observations of imide functionalities. To quantify the content of the different linear aldehydes (NIPTP and BTDTP), quantitative digestion ^{1}H NMR experiments were carried out using 1,4-dimethoxybenzene as internal patron (Table S1 and Figures S15–S21, Supporting Information). In this way, we observed that the relative percentages between the aldehydes are close to the nomenclature used in this study (NIP$_{X\%}$COF), which is based on the percentage of the NIP linker employed in the polymerization with reference to the stoichiometric reaction with maximum deviation from the ideal value ≈5%.

The porosity of the activated materials is evaluated using nitrogen sorption isotherms at 77 K (**Figure 2A**). As anticipated, the recorded isotherms exhibit a transition from a type IV isotherm to a type I isotherm with the increase of the number of **NIPTP** units, indicating that a transition from mesoporous to microporous materials is taking place due to the reduction of the pore size produced by the naphtalenimide moieties.[19] The surface areas of the polymers (Figure 2B) were calculated using the Brunauer-Emmet-Teller (BET) model, which exhibited the same trend as observed with the nitrogen uptake. Thus, the surface area decreases with an increase in **NIPTP** content in the moiety, transitioning from values of 1647 m^{2}g^{-1} for **NIP$_0$-COF** to 100 m^{2}g^{-1} for **NIP$_{100}$-COF** (Figure 2B; Figures S22–S27, Supporting Information). However, **NIP$_{25}$-COF** demonstrates an increase in surface area in comparison to **NIP$_{12}$-COF** and even **NIP$_0$-COF**. In line with this, the pore volume values (Figure 2B) at 0.95 p/p° exhibit a similar trend of progressively decreasing from **NIP$_0$-COF** (1.22 cm^{3}g^{-1}) to **NIP$_{100}$-COF** (0.09 cm^{3}g^{-1}), with the exception of **NIP$_{25}$-COF** (1.15 cm^{3}g^{-1}). Lastly, NLDFT calculations provided pore size distributions (Figure 2C; Figures S28–S33, Supporting Information), indicating a pore size of 3.2 nm for **NIP$_0$-COF**, which decreased progressively with higher percentages of **NIPTP** (Supporting Information). Crystallinity was studied with Powder X-Ray Diffraction (PXRD). Diffractograms (Figure 2D; Figures S34–S39, Supporting Information) showed signals ≈2.82, 3.96, 5.54, 8.28, 11.05, corresponding to (110), (200), (220), (330), and (440) facets.[19] As **NIPTP** percentage increases, signal intensity decreases and the Full-Width at Half Maximum (FWHM) increases, as shown in Figure 2B, with the progressively increasing content of a moiety with alkyl chains.[23]

Finally, to further validate the formation of the multivariate phases and exclude the possibility of crystalline domains of the **NIP$_0$-COF** mixed with NIPTP amorphous polymers, we conducted sub-stoichiometric reactions between BTDTP and TPAP under the conditions used for **NIP$_{50}$-COF** and **NIP$_{75}$-COF** but without the addition of NIPTP to the reaction medium (referred to as **TPAP-BTDTP$_{50}$** and **TPAP-BTDTP$_{25}$**, respectively). Notably, a significant loss of long-range ordering was observed in the

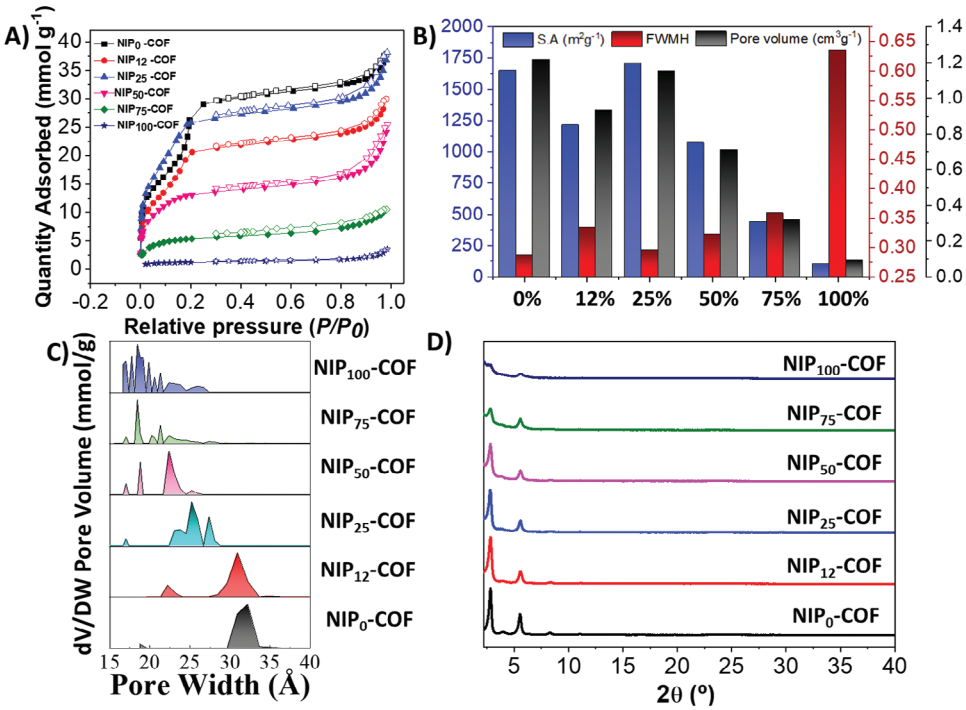

Figure 2. A) N_2 sorption isotherms at 77 K of **NIP$_{X\%}$-COFs** (filled and hollow symbols represent adsorption and desorption branches, respectively). B) Comparison of surface area (S.A), full width at half maximum (FWHM) and pore volume of the **NIP$_{X\%}$-COFs**. C) Comparison of pore size distributions. D) PXRD comparison of **NIP$_{X\%}$-COFs**.

diffractograms, confirming that the NIPTP and BTDTP linkers form a homogeneous and unique crystalline phase. The observed reduction in porosity can be attributed to the bulky size of the NIP moiety (Figure S40, Supporting Information).

A comprehensive series of Density Functional Theory (DFT) calculations was undertaken to investigate the structural characteristics of the **NIP$_{x\%}$-COF** compounds. The simulation results indicate that the 2D frameworks consistently exhibit exclusive rectangular D2 symmetry, characterized by monolayer lattice parameters perpendicular to the ***a*** and ***b*** axes of 45.14 and 48.16 Å, respectively (**Figure 3**) corresponding to the parent **NIP$_0$-COF** structure. The preferred stacking configuration is the eclipsed one in all cases (Figure S41, Supporting Information), with predicted π–π stacking interlayer distances of 3.62, 3.76, 3.81, 3.86 and 3.88 Å for the **NIP$_0$-COF**, **NIP$_{25}$-COF**, **NIP$_{50}$-COF**,**NIP$_{75}$-COF** and **NIP$_{100}$-COF**, respectively. Based on these structures, the theoretically simulated diffractograms exhibits an excellent agreement with the experimental one for the **NIP$_0$-COF** system, reinforcing the validity of the structure derived from simultaneous structure + cell DFT geometrical optimizations. As the interporous ligand content increases from 0 to 100%, the theoretical prediction deviates from the experimental due to differences between the average structure of the compounds in the experiment and the perfectly canonical conformation modelled from theory. It should be mentioned that despite the current simplified models may not capture the full complexity of each system, we believe it still provides a solid foundation for discussing the properties of these COFs. Finally, we have carried out Pawley refinements of the different COFs with the respective model, showing good agreement with the experimental data (Figures S42–S46, Supporting Information).

To analyze the influence of the contents of the two different linear dialdehydes, we have computed its two representative molecular fragments as shown in Figure S47 (Supporting Information) to perform a dimeric coupling study for all the combinations between them in both parallel and antiparallel conformations. The result of this theoretical analysis is shown in the figure, together with the computed coupling energies in kcal mol^{-1}. It is interesting to notice that all the dimeric structures analyzed yield favorable coupling energies ranging between −20.7 and −35.6 kcal mol^{-1} (negative sign here means favorable coupling), which manifests the tendency to stabilize under coupling. Besides, between the two (a, b) and (c, d) dimeric systems in Figure S47 (Supporting Information), the dimers prefer to couple in an antiparallel way, following the same tendency found for other COF systems.[24] On the contrary, for the case of the (e, f) dimer, the preferential configuration is the parallel one, due to the larger aromatic surface of the rylenimide moiety which favors the co-facial interaction. Finally, it should be noted that the parallel binding energies increase from a<c<d dimeric pairs, indicating that the introduction of the naphthaleneimide moieties could enhance the interlayer interactions. While stronger binding energies may facilitate dimer formation and COF crystallization, excessively strong interactions can inhibit the growth of larger crystallites by limiting the error-correction mechanisms. We hypothesize that, for this system, the optimum situation could be obtained in percentages ≈25% yielding lower FWMH values (Figure 2b) than expected, and thus, proportions above 50% of

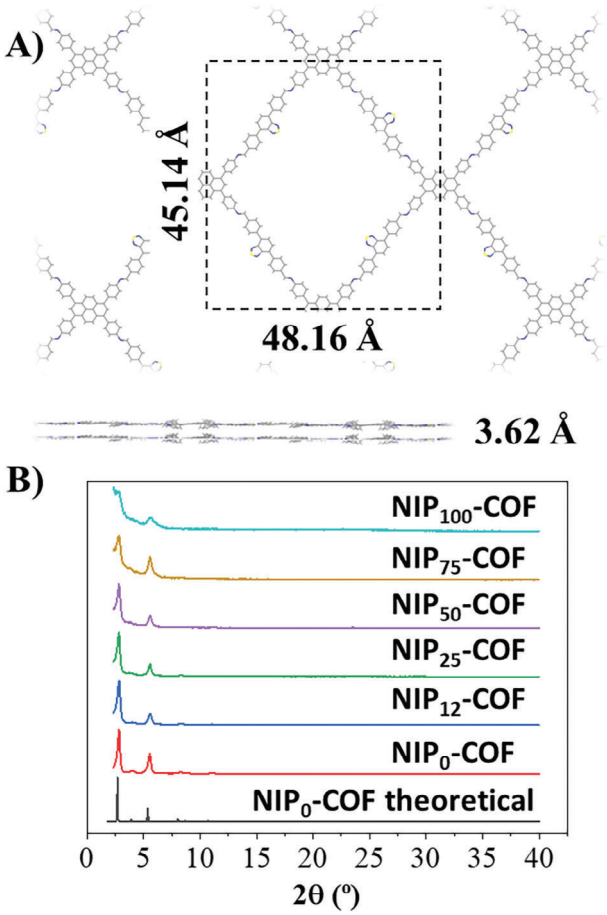

Figure 3. Simulated diffractograms obtained from the resulting DFT-optimized structures for: A) **NIP$_0$-COF** showing a top and side pictorial views of the structure and the resulting computed optimized unit cell with the preferential AA eclipsed interlayer stacking configuration. B) Comparison between experimental diffractograms of the **NIP$_{X\%}$-COFs** with the theoretical one calculated for **NIP$_0$-COF**.

the crystal growth can be reduced by the decreased reticulation processes.

Thermal stability was evaluated with Thermogravimetric Analysis (TGA), showing that all the COFs are stable until 410 °C (Figures S48–S53, Supporting Information). In addition, we carried out thermal stability tests by heating the COFs at 300 °C for 16 h under vacuum (see Supporting Information). After the experiments, the products were analyzed by FTIR confirming that the organic structure remains intact for all the products (Figure S54, Supporting Information). Moreover, PXRD analysis revealed that **NIP$_{X\%}$-COFs** (with X = 0, 12, 25 and 50) retains the diffraction maxima of the untreated COFs (Figure S55, Supporting Information) confirming their good thermal stability. The morphology of the samples was studied using Scanning Electron Microscopy (SEM) revealing a heterogeneous distribution of rod-like COF grains with lateral and width ≈65 nm (Figures S56–S61, Supporting Information). The materials were further studied with Transmission Electron Microscopy (TEM). Thus, COF suspensions were prepared (see Supporting Information),

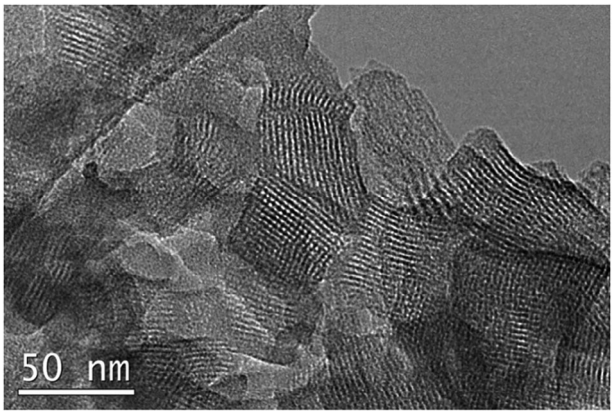

Figure 4. HR-TEM micrograph of **NIP$_{50}$-COF** (scale bar 50 nm).

and drop cast into TEM holders showed that the COFs retain the rod-like morphology registered in the scanning experiments.

Moreover, the TEM micrographs show the laminar nature of the materials (Figures S62–S67, Supporting Information). In addition, high-resolution TEM (HR-TEM) confirmed that the introduction of the naphthaleneimide moieties does not affect the morphology of the crystals (**Figure 4**; Figures S68–S72, Supporting Information). Thus, the high-resolution micrographs enable the observation of the highly ordered nanostructured materials, with intersecting nanopores with sizes ≈2.4 nm especially in the samples **NIP$_0$-COF** to **NIP$_{50}$-COF** where the pores are clearly visible. In the cases of **NIP$_{75}$-COF** and **NIP$_{100}$-COF** it is not possible to observe the nanopores due to pore saturation and reduced contrast caused by the naphthaleneimide moieties pendant inside these cavities.

UV–Vis spectra of the COF colloids revealed the absorption bands of the constitutional monomers (Figure S73, Supporting Information). As expected, upon introducing **NIPTP** into the framework structure, its corresponding absorption band (≈340 nm) is clearly visible in **NIP$_{100}$-COF**. Furthermore, this effect was further investigated by comparing COFs with different percentages of **NIPTP**. With increasing **NIPTP** content, the intensity of its corresponding absorption band increases, while that of **BTDTP** (≈398 nm) decreases.

2.2. Photoconductivity Studies

It was established that the charge carrier transport pathways in D-A based COFs can be tuned by varying the building blocks.[25] In these D-A based **NIP$_{X\%}$-COFs**, two types of conduction pathways can be realized: a hole transport pathway through the stacking of the electron rich pyrene cores, or an electron transport pathway via the stacking of benzothiazole/naphthaleneimide moieties. Moreover, lowering of the band gap of the semiconducting material improves the charge carrier generation yield due to the higher yield of hot excitons. The efficient charge separation between donor and acceptor units leads to a stronger charge migration.[26] On the other hand, the photoconductivity of multivariate COFs measured by FP-TRMC techniques often showed lower photoconductivity than pristine unmixed COFs due to the random arrangement of chromophores/linkers within

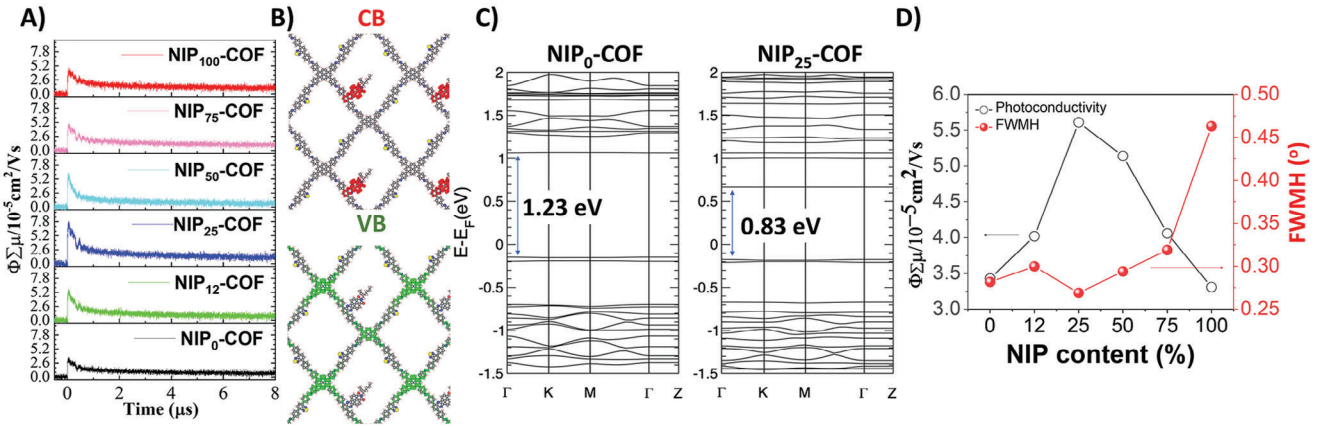

Figure 5. A) Kinetic traces of conductivity transients observed for **NIP$_{X\%}$-COFs** samples bound on PMMA matrix upon excitation of 355 nm laser pulses at 9.1×10^{15} photons cm^{-2}. B) 3D isosurfaces (both with an isovalue of 0.0001 a.u.) corresponding to the valence (VB) and conduction (CB) bands are shown for the **NIP$_{25}$-COF**. C) Calculated band structure for **NIP$_0$-COF** and **NIP$_{25}$-COF** crystal bulks indicating the corresponding band gap. D) Comparison of Kinetic traces of conductivity with FWHM values.

the frameworks.[26] To determine the intrinsic photoconductivity and the nature of the conducting species of these COFs, flash-photolysis time-resolved microwave conductivity (FP-TRMC) was employed upon 355 nm laser excitation with a photon density of 9.1×10^{15} photons cm^{-2} pulse^{-1} under N_2 atmosphere. It measures the maximum photoconductivity as $\phi\Sigma\mu$ from the rise and decay transient, where ϕ is the charge carrier generation quantum yield and $\Sigma\mu$ is the sum of the photo-injected charge carrier mobilities of mobile electrons and holes.[16f]

Figure 5A depicts the kinetic traces of photoconductivity of **NIP$_{X\%}$-COFs**. Here we observed that the photoconductivity of these COFs increases with a gradual increase of **NIPTP** content into the framework up to 25% as the band gap decreases (1.95 eV for **NIP$_0$-COF** to 1.77 eV for **NIP$_{75}$-COF**) with the percentage of the naphtaleneimide (**NIP**) content owing to the higher electron accepting ability of the naphtaleneimide unit than benzothiazole moiety. This phenomenon is also supported by the band structure diagram of **NIP$_{25}$-COF**, in which the electron density of the conduction band is majorly located in the naphthaleneimide moieties rather than benzothiazole moieties (Figure 5B). Moreover, it is well established that the shorter intermolecular π–π distances between the COF layers led to a higher charge carrier mobility.[27] In these **NIP$_{X\%}$-COFs**, as the percentage of the bulky **NIP** moiety increases within the frameworks, the interlayer distance increases from 3.62 Å (**NIP$_0$-COF**) to 3.88 Å (**NIP$_{100}$-COF**). Thus, the maximum photoconductivity of 7.9×10^{-5} cm^2 V^{-1} s^{-1} was observed for **NIP$_{25}$-COF** owing to the lowering of band gap energy, and relatively shorter interlayer distance while maintaining the crystallinity and the conducting pathways.

A further increase of **NIP** percentage (beyond 25%) led to a decrease in photoconductivity which may be due to the larger interlayer distance and the disruption of conducting pathways as the concentration of the bulky NIPTP increases in the frameworks (**NIP$_{50}$-COF** and **NIP$_{100}$-COF**). To check the major of conducting species (hole or electron), a photoconductivity experiment was performed in the presence of SF_6 (electron scavenger) with one of the representative COFs with the highest crystallinity. The negligible change in decay kinetics indicated a hole-conducting nature of the frameworks which is also supported by the iodine doping experiment (*vide supra*) (Figure S74, Supporting Information).[26] We hypothesize that the presence of the **NIPTP** acts as a "dopant" in the crystalline frameworks to reduce the material's bandgap. To study this, a large battery of DFT based calculations has been carried out to analyze the effects of the presence of the benzothiadiazole and naphthalenimide moieties spread along the extended frameworks. First, the analysis of the topologies of the valence and conduction bands revealed that the introduction of the NIPTP linker produces great segregation of the conduction (CB) and valence (VB) bands. Thus, for the **NIP$_{X\%}$-COFs** (where X > 0) the conduction band is located in the naphthaleneimide moieties, while the valence band is spread in the aromatic pyrene knots (Figure 5B). From this data, the computed band structure for **NIP$_0$-COF** and **NIP$_{25}$-COF** crystal bulks revealed that the compounds are theoretically predicted as narrow-gap semiconductors. Interestingly, the introduction of the **NIPTP** moieties reduces the bandgap of the materials, demonstrating that the introduction of the naphthalenimide acceptors effectively modulates optoelectronical properties of these materials (Figure 5B). This was further studied by the collection of the diffuse-reflectanceUV–vis spectra (DR-UV–vis) of the **NIP$_{X\%}$-COFs** and representing the corresponding Tauc-Plots to analyze the optical bandgap of these materials (Figures S75 and S76, Supporting Information). From this data we could observe that the increasing content of naphthalenimide moieties lowered the gap from 1.95 eV for **NIP$_0$-COF** to 1.77 eV for **NIP$_{75}$-COF**, corroborating the hypothesis stated above. In addition, the optical bandgap for **NIP$_{100}$-COF** increased to 1.84 eV, probably due to the low crystallinity of this system. It is worth mentioning that, with the increasing content of **NIPTP**, greater orbital segregation would be anticipated, which could be advantageous in enhancing electron-hole separation and preventing recombination.[16b,28] However, the increasing content of the naphthalenlimide affected the crystallization processes, leading to less ordered π-arrays and hindering the migration processes. Finally, a comparison between the photoconductivity and FWHM values revealed a non-linear relationship between both magnitudes (Figure 5D). This is especially evident when comparing **NIP$_{12}$-COF** and **NIP$_{50}$-COF**, as, despite almost identical FWHM values, the photoconductivity

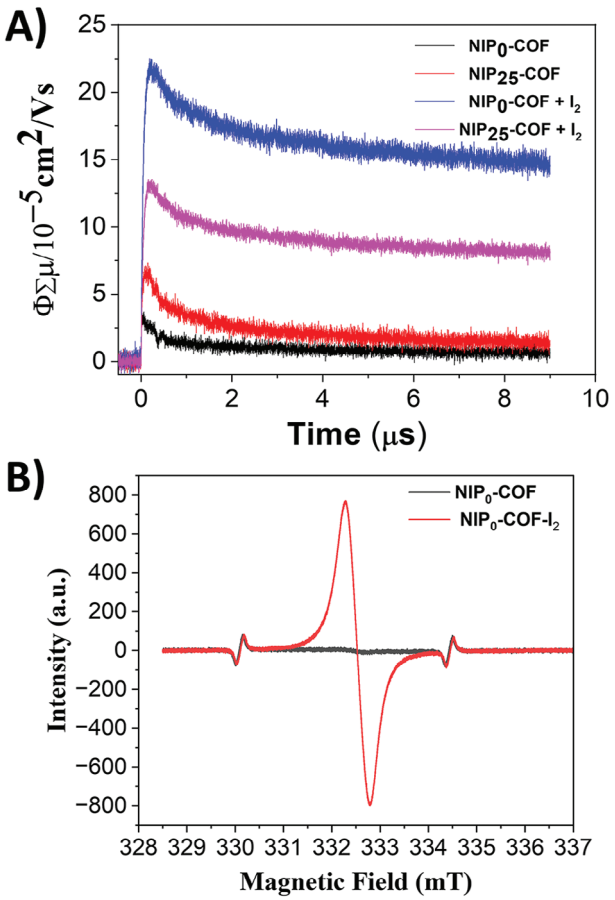

Figure 6. A) Kinetic traces of conductivity transients observed for **NIP$_0$-COF** and **NIP$_{25}$-COF** before and after I_2 doping. B) EPR spectra of **NIP$_0$-COF** before and after I_2 doping.

is higher for the COF with a higher amount of naphtalenimide (50%). Additionally, the photoconductivity of **NIP$_{75}$-COF** is comparable to that of **NIP$_{12}$-COF**, despite slightly higher FMWH values. This discrepancy is more pronounced when comparing the highly crystalline **NIP$_0$-COF** with the less ordered **NIP$_{100}$-COF**, indicating that the differences in photoconduction cannot solely be attributed to variations in crystallinity among these samples.

The presence of electron-rich pyrene moiety and the predominance of hole-conducting charge carrier species over electrons motivates us to investigate the electrical conductivity of these COFs with I_2 doping.[29] To achieve this, the film samples used for TRMC measurement are immersed in an I_2 chamber. To remove the excess I_2 molecules that may have been absorbed into the pores, the doped films are subsequently dried in a vacuum at 50^{0}C for 1 hr. From **Figure 6A**, it was observed that doped **NIP$_{X\%}$-COFs** exhibit an enhancement in photoconductivity compared to their respective pristine analogs. Among them, **NIP$_0$-COF** showed a higher enhancement (six times) in conductivity than the others, possibly due to the higher surface area of **NIP$_0$-COF**, which facilitated the adsorption of I_2 into the pores (Table S3, Supporting Information). Furthermore, in **NIP$_0$-COF**, the absence of the strong electron-accepting **NIPTP** moiety in the framework (all BTDTP linker), results in the pyrene core being more electron-rich, thereby favoring its oxidation with I_2. Formation of oxidized species after doping is also confirmed from the electron paramagnetic resonance (EPR) spectra (Figure 6B). In the EPR spectra of the doped COFs, the appearance of a sharp peak at g = 2.0084, indicate the formation of pyrene radical cation species.[28] The comparison of the PXRD and FTIR spectra before and after doping indicated the retention of crystallinity and functionality after I_2 doping (Figures S77 and S78, Supporting Information). The nature of the reduced I_2 species is further confirmed by Raman spectroscopy. Thus, the emergence of a prominent peak at 158 cm^{-1} after doping suggested the existence of I_5^- species, formed following a charge transfer complex (Figure S79, Supporting Information).[30]

3. Conclusion

A series of six **NIP$_{X\%}$-COFs** has been developed through the three-component reaction of **TPAP** as an electron-rich tetragonal knot with two electron-deficient moieties (**BTDTP** and **NIPTP**) in varying proportions. This approach allowed for precise customization of the optoelectronic properties of isotopological frameworks while maintaining their structural integrity. The formation of a D-A heterojunction by combining TPAP with different acceptors made these materials ideal for charge carrier transport. In this study, TRMP was utilized with a 355 nm laser to evaluate these materials, revealing that doping with naphthalenimide moieties at 25% (**NIP$_{25}$-COF**) resulted in the highest photoconductivity with a value of 7.9×10^{-5} cm^2 V^{-1} s^{-1}. The analysis demonstrated a relationship between photoconductivity values and the increasing content of the **NIPTP** linker, which was supported by DFT-based calculations and crystal characteristics of the networks. Further investigations indicated that hole transport was the preferred conducting pathway due to possible antiparallel stacking of the accepting units. In conclusion, the three-component synthesis of COFs has proven to be a versatile method for producing tailored materials and enhancing pore-complexity.

Supporting Information

Supporting Information is available from the Wiley Online Library or from the author.

Acknowledgements

M.G.-L., M.M.-F., and R.P.P. contributed equally to this work. This work was financially supported by Ministerio de Ciencia e Innovación of Spain MICINN (Grants TED2021-129886B-C43, PID2022-138908NB-C33, PID2020-113142RB-C21, RED2022-134503-T, and PLEC2021-007906), by Comunidad de Madrid (Grant TEC2024/ECO-332) and by The Japan Society for the Promotion of Science (Grants 22H00314, 20H05867, and 20H05862) and Japan Science and Technology Agency (Grant number: JPMJCR23O3). R.P.P. is thankful for a fellowship from JSPS (ID No. P22045). J.I.M. also acknowledges funding by Comunidad de Madrid (Grants S2018/NMT-4367 and Y2020/NMT-6469).

Conflict of Interest

The authors declare no conflict of interest.

Data Availability Statement

The data that support the findings of this study are available from the corresponding author upon reasonable request.

Keywords

benzothiadiazole, COF, hole, naphthaleneimide, photoconductivity

Received: July 23, 2024
Revised: October 18, 2024
Published online:

[1] a) T. Wang, S. P. S. Fernandes, J. Araújo, X. Li, L. M. Salonen, B. Espiña, *J. Hazard. Mater.* **2023**, *452*, 131247; b) W. Guo, J. Liu, H. Tao, J. Meng, J. Yang, Q. Shuai, Y. Asakura, L. Huang, Y. Yamauchi, *Adv. Mater.* **2024**, *36*, 2405399.

[2] a) M. Martínez-Fernández, E. Martínez-Periñán, J. I. Martínez, M. Gordo-Lozano, F. Zamora, J. L. Segura, E. Lorenzo, *ACS Sustainable Chem. Eng.* **2023**, *11*, 1763; b) M. Martínez-Fernández, J. L. Segura, *ChemSusChem.* **2024**, *17*, e202400558.

[3] a) D. Li, C. Li, L. Zhang, H. Li, L. Zhu, D. Yang, Q. Fang, S. Qiu, X. Yao, *J. Am. Chem. Soc.* **2020**, *142*, 8104; b) J. Xue, Z. Sun, B. Sun, C. Zhao, Y. Yang, F. Huo, A. Cabot, H. K. Liu, S. Dou, *ACS Nano.* **2024**, *18*, 17439.

[4] a) K. Geng, T. He, R. Liu, S. Dalapati, K. T. Tan, Z. Li, S. Tao, Y. Gong, Q. Jiang, D. Jiang, *Chem. Rev.* **2020**, *120*, 8814; b) Y. Chen, D. Jiang, *Acc. Chem. Res.* **2024**, *57*, 3182.

[5] a) L. Deng, Z. Ding, X. Ye, D. Jiang, *Acc. Mater. Res.* **2022**, *3*, 879; b) W. Lee, H. Li, Z. Du, D. Feng, *Chem. Soc. Rev.* **2024**, *53*, 8182.

[6] a) S. Liu, M. Liu, X. Li, Q. Xu, Y. Sun, G. Zeng, *J. Mater. Chem. A Mater.* **2023**, *11*, 13965; b) L. Zhang, Q.-Q. Zheng, S.-J. Xiao, J.-Q. Chen, W. Jiang, W.-R. Cui, G.-P. Yang, R.-P. Liang, J.-D. Qiu, *J. Chem. Eng.* **2021**, *426*, 131865; c) H. Ran, Q. Xu, Y. Yang, H. Li, J. Fan, G. Liu, L. Zhang, J. Zou, H. Jin, S. Wang, *ACS Catal.* **2024**, *14*, 11675.

[7] J. L. Segura, S. Royuela, M. M. Ramos, *Chem. Soc. Rev.* **2019**, *48*, 3903.

[8] a) L. Frey, O. Oliveira, A. Sharma, R. Guntermann, S. P. S. Fernandes, K. M. Cid-Seara, H. Abbay, H. Thornes, J. Rocha, M. Döblinger, T. Kowalczyk, A. Rao, L. M. Salonen, D. D. Medina, *Angew. Chem., Int. Ed.* **2023**, *62*, 202302872; b) D. N. Bunck, W. R. Dichtel, *Chem.-Eur. J.* **2013**, *19*, 818.

[9] Y. Zeng, R. Zou, Z. Luo, H. Zhang, X. Yao, X. Ma, R. Zou, Y. Zhao, *J. Am. Chem. Soc.* **2015**, *137*, 1020.

[10] a) H. Yazdani, S. E. Hooshmand, R. S. Varma, *Org. Chem. Front.* **2022**, *9*, 4178; b) M. Wang, T. Zeng, Y. Yu, X. Wang, Y. Zhao, H. Xi, Y. Zhang, *J. Am. Chem. Soc.* **2024**, *146*, 1035; c) L. S. J. Yue, X. Ding, Y. Wang, P. Yang, Y. Ma, B. Tang, *Anal. Chem.* **2022**, *94*, 11062; d) Y. Yang, M. Faheem, L. Wang, Q. Meng, H. Sha, N. Yang, Y. Yuan, G. Zhu, *ACS Cent. Sci.* **2018**, *4*, 748; e) T. Prieto, C. Ponte, R. Guntermann, D. D. Medina, L. M. Salonen, *Chem.-Eur. J.* **2024**, *30*, 202401344.

[11] a) Z. Li, K. Geng, T. He, K. T. Tan, N. Huang, Q. Jiang, Y. Nagao, D. Jiang, *Angew. Chem., Int. Ed.* **2021**, *60*, 19419; b) C. Han, J. Guo, S. Sun, Z. Wang, L. Wang, X. Liu, *Small.* **2024**, 2405887; c) C.-W. Wu, C. E. Cai, Y.-C. Feng, Z.-T. Chen, B.-T. Liu, H. Yang, S.-Y. Suen, D.-W. Kuo, R.-H. Lee, *ACS Appl. Nano. Mater.* **2024**, *7*, 23087.

[12] a) M. A. Ibrahem, E. Verrelli, A. M. Adawi, J.-S. G. Bouillard, M. O'Neill, *ACS Omega.* **2024**, *9*, 10169; b) N. Keller, T. Bein, *Chem. Soc. Rev.* **2021**, *50*, 1813; c) C. Wu, Y. Liu, H. Liu, C. Duan, Q. Pan, J. Zhu, F. Hu, X. Ma, T. Jiu, Z. Li, Y. Zhao, *J. Am. Chem. Soc.* **2018**, *140*, 10016.

[13] a) S. Wan, J. Guo, J. Kim, H. Ihee, D. Jiang, *Angew. Chem., Int. Ed.* **2009**, *48*, 5439; b) M. Dogru, M. Handloser, F. Auras, T. Kunz, D. Medina, A. Hartschuh, P. Knochel, T. Bein, *Angew. Chem., Int. Ed.* **2013**, *52*, 2920; c) Y.-H. Chen, C.-F. Huang, T.-Y. Lo, M. Chandra Sil, C.-M. Chen, *J. Photochem. Photobiol. A Chem.* **2025**, *459*, 116052; d) H. R. Abuzeid, D. J. J. Tay, B. Febriansyah, A. Kanwat, T. Salim, A. A. Zhumekenov, S. A. Pullarkat, N. Mathews, *Small Methods.* **2024**, 2400666.

[14] F. Suárez-Blas, L. Pandolfi, M. J. Alonso-Navarro, S. Riera-Galindo, J. I. Martínez, B. Dörling, A. Funes, A. Harillo-Baños, E. Venuti, M. M. Ramos, M. Campoy-Quiles, J. L. Segura, *Adv. Energy Sustain. Res.* **2024**, *5*, 2400028.

[15] a) S. Jin, X. Ding, X. Feng, M. Supur, K. Furukawa, S. Takahashi, M. Addicoat, M. E. El-Khouly, T. Nakamura, S. Irle, S. Fukuzumi, A. Nagai, D. Jiang, *Angew. Chem., Int. Ed.* **2013**, *52*, 2017; b) R. Guntermann, D. Helminger, L. Frey, P. M. Zehetmaier, C. Wangnick, D. D. Medina, T. Bein, A. Singh, T. Xue, Tunable, *Angew. Chem., Int. Ed.* **2024**, e202407166.

[16] a) K. D. Kwon, K. Refson, G. Sposito, *Phys. Rev. Lett.* **2008**, *100*, 146601; b) L. Stegbauer, S. Zech, G. Savasci, T. Banerjee, F. Podjaski, K. Schwinghammer, C. Ochsenfeld, B. V. Lotsch, *Adv. Energy Mater.* **2018**, *8*, 1703278; c) F. Yu, W. Liu, B. Li, D. Tian, J. Zuo, Q. Zhang, *Angew. Chem., Int. Ed.* **2019**, *58*, 16101. d) G. Bian, J. Yin, J. Zhu, *Small.* **2021**, *17*, 2006043. e) S. Kim, H. Jung, M. S. Okyay, H. Noh, S. Chung, Y. H. Kim, J. Jeon, B. M. Wong, K. Cho, J. Seo, J. Yoo, J. Baek, *Angew. Chem., Int. Ed.* **2023**, *62*, 202310560. f) S. Ghosh, Y. Tsutsui, T. Kawaguchi, W. Matsuda, S. Nagano, K. Suzuki, H. Kaji, S. Seki, *Chem. Mater.* **2022**, *34*, 736. g) S. Fu, E. Jin, H. Hanayama, W. Zheng, H. Zhang, L. Di Virgilio, M. A. Addicoat, M. Mezger, A. Narita, M. Bonn, K. Müllen, H. I. Wang, *J. Am. Chem. Soc.* **2022**, *144*, 7489.

[17] L. Li, W. Fang, P. Zhang, J. Bi, Y. He, J. Wang, W. Su, *J. Mater. Chem. A Mater.* **2016**, *4*, 12402.

[18] Q. Li, J. Wang, Y. Zhang, L. Ricardez-Sandoval, G. Bai, X. Lan, *ACS Appl. Mater. Interfaces.* **2021**, *13*, 39291.

[19] Z. Li, Y. Zhi, P. Shao, H. Xia, G. Li, X. Feng, X. Chen, Z. Shi, X. Liu, *Appl. Catal. B.* **2019**, *245*, 334.

[20] N. Keller, D. Bessinger, S. Reuter, M. Calik, L. Ascherl, F. C. Hanusch, F. Auras, T. Bein, *J. Am. Chem. Soc.* **2017**, *139*, 8194.

[21] M. J. Alonso-Navarro, A. Harbuzaru, M. Martínez-Fernández, P. Pérez Camero, J. T. López Navarrete, M. M. Ramos, R. P. Ortiz, J. L. Segura, *J. Mater. Chem. C.* **2021**, *9*, 7936.

[22] H. Xu, J. Gao, D. Jiang, *Nat. Chem.* **2015**, *7*, 905.

[23] A. De, S. Haldar, S. Michel, L. Shupletsov, V. Bon, N. Lopatik, L. Ding, L. M. Eng, G. K. Auernhammer, E. Brunner, A. Schneemann, *Chem. Mater.* **2023**, *35*, 3911.

[24] Z. Mu, Y. Zhu, B. Li, A. Dong, B. Wang, X. Feng, *J. Am. Chem. Soc.* **2022**, *144*, 5145.

[25] a) X. Feng, L. Liu, Y. Honsho, A. Saeki, S. Seki, S. Irle, Y. Dong, A. Nagai, D. Jiang, *Angew. Chem.* **2012**, *124*, 2672. b) E. L. Spitler, B. T. Koo, J. L. Novotney, J. W. Colson, F. J. Uribe-Romo, G. D. Gutierrez, P. Clancy, W. R. Dichtel, *J. Am. Chem. Soc.* **2011**, *133*, 19416. c) X. Feng, L. Chen, Y. Honsho, O. Saengsawang, L. Liu, L. Wang, A. Saeki, S. Irle, S. Seki, Y. Dong, D. Jiang, *Adv. Mater.* **2012**, *24*, 3026.

[26] S. Ghosh, A. Nakada, M. A. Springer, T. Kawaguchi, K. Suzuki, H. Kaji, I. Baburin, A. Kuc, T. Heine, H. Suzuki, R. Abe, S. Seki, *J. Am. Chem. Soc.* **2020**, *142*, 9752.

[27] S. Seki, R. Prasad Paitandi, W. Choi, S. Ghosh, T. Tanaka, *Acc. Chem. Res.* **2024**, *57*, 2665.

[28] S. Ghosh, Y. Tsutsui, K. Suzuki, H. Kaji, K. Honjo, T. Uemura, S. Seki, *Mol. Syst. Des. Eng.* **2019**, *4*, 325.

[29] E. Jin, M. Asada, Q. Xu, S. Dalapati, M. A. Addicoat, M. A. Brady, H. Xu, T. Nakamura, T. Heine, Q. Chen, D. Jiang, *Science.* **2017**, *357*, 673.

[30] R. Li, G. Xing, H. Li, S. Li, L. Chen, *Chin. Chem. Lett.* **2023**, *34*, 107454.